

Article

Discovery of Spontaneous De-Interpenetration Through Charged Point-Point Repulsions

Sylvia L. Hanna¹, Saumil Chheda^{2,3}, Ryther Anderson⁴, Debmalya Ray³, Christos D. Malliakas¹, Julia G. Knapp¹, Ken-ichi Otake¹, Peng Li¹, Penghao Li¹, Xingjie Wang¹, Megan C. Wasson¹, Katarina Zosel⁴, Austin M. Evans¹, Lee Robison¹, Timur Islamoglu¹, Xuan Zhang¹, William R. Dichtel¹, J. Fraser Stoddart¹, Diego A. Gomez-Gualdron⁴, Laura Gagliardi⁵, Omar K. Farha^{1,6,*}

¹Department of Chemistry and International Institute for Nanotechnology, Northwestern University, 2145 Sheridan Rd, Evanston, IL 60208, USA.

²Department of Chemical Engineering and Materials Science, University of Minnesota, Twin Cities, 421 Washington Ave SE, Minneapolis, MN 55455, USA.

³Department of Chemistry, Chemical Theory Center, and Minnesota Supercomputing Institute, University of Minnesota, Pleasant St SE, Minneapolis, MN 55455, USA.

⁴Department of Chemical and Biological Engineering, Colorado School of Mines, Golden, CO 80401, USA.

⁵Department of Chemistry, Pritzker School of Molecular Engineering, James Franck Institute, and Chicago Center for Theoretical Chemistry, The University of Chicago, 5735 S Ellis Ave, Chicago, IL 60637, USA.

⁶Department of Chemical and Biological Engineering, Northwestern University, 2145 Sheridan Rd, Evanston, IL 60208, USA.

*Correspondence and Lead Contact: o-farha@northwestern.edu

SUMMARY

Energetically driven reduction of porosity through entanglement is ubiquitous in Nature and synthetic systems. This entanglement decreases valuable internal pore space useful for applications such as catalysis, storage, and sensing. Here, we describe the discovery of spontaneous de-interpenetration in a 6-fold interpenetrated uranium-based metal-organic framework (MOF), NU-1303-6. De-interpenetration transforms NU-1303-6 (14.2 and 19.8 Å pores) to its larger pore (40.7 Å) non-interpenetrated counterpart which possesses a record high 96.6% void fraction and 9.2 cm³g⁻¹ pore volume. Density functional theory calculations reveal that charged point-point repulsions between anionic, closely positioned uranium-based nodes drive this phenomenon. These repulsions compete with water molecules that hydrogen-bond nearby networks together, favoring interpenetration. Controlling the interplay between these intermolecular forces enables the reversal of omnipresent energetic equilibria, leading to thermodynamically favored open pore structures. The discovery of charged point-point repulsion will likely lead to the re-evaluation of non-interpenetrated network design, synthesis, and wide-reaching applications.

KEYWORDS

Metal-organic framework, uranium, charged point-point repulsion, interpenetration, entanglement, spontaneous

INTRODUCTION

Natural and synthetic entangled molecular systems are invariably considered more stable than their non-interlocked counterparts. This understanding originates from the fact that non-covalent interactions such as hydrogen bonding, π - π stacking, and Van der Waals forces are maximized in tightly packed systems with minimal porosity, thus forming energetically favored thermodynamic products¹⁻³. Tightly packed or interlocked structures inherently have less void space compared to their kinetically favored, open counterparts, which reduces the accessible surface for applications of wide-reaching importance such as gas storage^{4,5}, chemical sensing^{6,7}, bio-molecule encapsulation⁸, medical diagnostics⁹, electronics¹⁰, and catalysis¹¹. To maximize the application relevance of porous materials, significant effort has been devoted to synthesizing kinetically preferred and packing-frustrated open-pore materials¹²⁻¹⁴. Here, we detail the discovery of a phenomenon that we term charged point-point repulsion (CPPR), which reverses the universal thermodynamics of void space and consequently leads to spontaneous de-interpenetration of interlinked networks.

We demonstrate this phenomenon through the spontaneous de-interpenetration of a 6-fold interpenetrated metal-organic framework (MOF)¹⁵⁻¹⁸, NU-1303-6, to its entirely non-interpenetrated counterpart. NU-1303-6 initially self-assembles as a densely intercalated periodic system of organic linkers and anionic uranium-based nodes^{19,20}, which are held in close proximity. The short distance between anionic uranyl nodes leads to CPPR-driven spontaneous de-interpenetration, thus reversing the pervasive thermodynamics of porous structures and generating a large-pore open structure (40 Å pore) with record high free void space (96.6%) and pore volume (9.2 cm³g⁻¹) from an initially nanoporous assembly (<20 Å pores).

Our results reveal how spontaneous de-interpenetration transforms initially crowded systems to thermodynamically favorable products with valuable free internal pore space, often coveted in porous material applications where interpenetration reduces porosity²¹. Additionally, spontaneous de-interpenetration in the absence of external stimuli simplifies the cumbersome process of designing materials that do not interpenetrate, as well as the design of syntheses where metastable products are targeted^{22,23}.

RESULTS AND DISCUSSION

Discovery of De-Interpenetration

We developed a solvothermal synthesis for NU-1303-6, and from single-crystal X-ray diffraction (SCXRD), we found the NU-1303-6 node consists of the uranyl unit²⁴—a single U(VI) atom bound to two axial oxygen atoms—coordinated by six equatorial oxygen atoms (Fig. 1A). These equatorial oxygen atoms originate from three separate ditopic, 2,2'-dimethyl-biphenyl-4,4'-dicarboxylic acid (DMBP) linkers (Figs. 1B, S1-S2, Scheme S1), each of which binds bidentately to the uranyl unit. The uranyl-based node thus holds a -1 formal charge, making the overall framework anionic ($(\text{H}^{+}_{0.9}\text{K}^{+}_{0.1}[\text{UO}_2(\text{DMBP})_{1.5}]^{-})$ or $(\text{H}_3\text{O}^{+})_{0.9}\text{K}^{+}_{0.1}[\text{UO}_2(\text{DMBP})_{1.5}]^{-}$, Figs. S9-S11, Table S2). The methyl groups located on the biphenylene linkers force rotation around the central carbon-carbon bond, making these building blocks self-assemble into a three-dimensional, srs-topology MOF (Fig. S7-S8, Table S1)²⁵. Each srs cage is 37.7 Å in diameter (Fig. 1C), and a single extended network of NU-1303-6 is observed in Figure 1D. Six of these identical networks intertwine (Fig. 1G) to form NU-1303-6, one of the highest-fold interpenetrated uranium MOFs reported to date, featuring 14.4 Å and 19.2 Å cages (Fig. 1F). Throughout the extended structure of NU-1303-6, there are two reoccurring motifs where anionic nodes on individual networks are separated by close distances. In one motif, the nodes spatially orient in a parallel arrangement, where the closest U-U distance is 9.7 Å (M1). In the other motif, the nodes spatially orient in a perpendicular arrangement, where the closest U-U distance is 8.1 Å (M2) (Fig. 1E). This structural analysis reveals that anionic NU-1303-6 adopts a crowded, interpenetrated configuration but is based upon an open network topology.

After soaking NU-1303-6 in *N,N*-dimethylformamide (DMF) for 96 hours, we removed the solvent in the pores by activation using supercritical CO₂²⁶ followed by thermal activation at 50 °C. We obtained the nitrogen adsorption-desorption isotherm of NU-1303-6, and determined its Brunauer-Emmett-Teller (BET) area²⁷ to be 1735 m²g⁻¹ and its pore volume to be 0.86 cm³g⁻¹. The nitrogen isotherm (Figs. 2D, S12, Table S3) possesses steps at relative pressures (P/P_0) of 0.009 and 0.070, corresponding to 14.2 Å and 19.8 Å pores (Figs. 2G, S13). These align well with the pore sizes determined from the single-crystal structure (Fig. 1F). The calculated geometric surface area for NU-1303-6 reveals a higher expected BET area and pore volume of 2340 m²g⁻¹ and 1.2 cm³g⁻¹, respectively (Tables S4-S5). We thus activated the material with 74% of the calculated geometric surface area, an occurrence which has also been observed in previous studies²⁰.

We discovered a drastic structural change in NU-1303-6 after we left the MOF to soak in DMF for 144 days at room temperature. The isotherm obtained after activation no longer indicated two steps at low relative pressure, but instead acquired one large step at $P/P_0 = 0.36$, an increase in pore volume to 2.25 cm³g⁻¹, and a decrease in BET area to 1525 m²g⁻¹ (Figs. 2F, S36, Table S3). Additionally, the pore size distribution revealed a much larger 40.7 Å pore (Fig. 2I). The significant increase in pore volume and pore size, coupled with the concurrent change in BET area, indicate the removal of framework walls. We hypothesized that this unanticipated phenomenon could be explained by de-interpenetration of 6-fold interpenetrated NU-1303-6 to its completely non-interpenetrated counterpart (NU-1303-1).

In search of more evidence to support this observation, we captured an intermediate three-fold interpenetrated single-crystal structure of NU-1303 (NU-1303-3) after soaking the NU-1303-6 crystals in DMF for 29 days (Figs. 2B, S28-S29, Tables S1, S12). Additionally, single-crystals of NU-1303-1 were preserved after soaking NU-1303-6 in DMF for 946 days (Fig. S30, Supplemental Data: NU-1303-1_Upositions). Since the low resolution of the NU-1303-1 SCXRD data only revealed the uranium positions instead of the full structure, we additionally modeled NU-1303-1 in Materials Studio by removing 5 of the 6 srs networks from NU-1303-6 while retaining the same topology and unit cell parameters (Figs. 2C, S31, Supplemental Data: NU-1303-1_Model). To ensure that this model matched the SCXRD data, we paired the extinction analyses from SCXRD with Le Bail analysis of a NU-1303-1 powder sample (Fig. S32), and we generated lattice parameters for the experimental structure. These experimental parameters matched those from the modeled structure precisely (Tables S8-S9). In this way, the SCXRD uranium positions of NU-1303-1 were validated both experimentally through powder refinement and computationally through Materials Studio modeling. The simulated PXRD generated from the single-crystal data also matches well with the simulated PXRD generated from the structural model (Fig. S33). Collectively, these findings are consistent with the presence of NU-1303-1.

While one might imagine that de-interpenetration etches away at portions of all 6 frameworks rather than removing 5 entire frameworks, this NU-1303-1 structure confirms that etching is not operative. Additionally, we anticipate that de-interpenetration *via* etching would result in a material with a wide distribution of multiple continuous pore sizes²⁸. However, we observe only one pore size by gas physisorption (40 Å, Fig. 2I) which matches well with the structure solution (37.7 Å) and further confirms that complete de-interpenetration from a 6-fold interpenetrated MOF to its non-interpenetrated counterpart occurs.

We obtained further evidence for de-interpenetration from an isotherm of NU-1303-6 soaked in DMF for an intermediate amount of time (17 days) which showed intermediate (higher than NU-1303-6, but lower than NU-1303-1) pore volume and pore-size distributions (Figs. S25-S27, Table S3). Additionally, evidence for de-interpenetration was also observed through the appearance of uranium in the DMF soaking solution, detected *via* inductively coupled plasma-mass spectrometry and ultraviolet-visible spectroscopy (Fig. S24).

Because simulated powder X-ray diffraction (PXRD) patterns of NU-1303-6, NU-1303-3, and NU-1303-1 all display similar peak positions (Fig. 2E), distinguishing interpenetration levels using PXRD peak positions is not feasible. Additionally, peak intensity provides little structural

information, as the 150–200 μm crystallite size (Fig. S6) introduces preferred orientation. Instead, we analyzed peak splitting to distinguish interpenetration level by PXRD. While the experimental NU-1303-6 PXRD peak positions prior to activation match the simulated patterns (Fig. 2E), after activation, the first two major PXRD peaks split (Fig. 2H). In contrast, NU-1303-1 exhibited no peak splitting after activation and matched well with the simulated NU-1301-1 pattern (Figs. 2H, S35). Thus, peak splitting after activation is an indicator of NU-1303-6, while the absence of peak splitting following activation suggests the presence of NU-1303-1. These findings are consistent with the interpenetration levels observed from nitrogen physisorption. This evidence supports de-interpenetration (Fig. 2A-C) in the absence of external stimuli. To identify the structural changes which cause peak splitting in NU-1303-6 after activation, we generated PXRD patterns and structural models that matched the experimental patterns of NU-1303-6 after activation (Supplemental Data: NU-1303-6_EtOH, NU-1303-6_Act, Fig. S15). This was performed by varying the lattice parameters of the simulated unit cells to maximize peak overlap between the experimental and simulated patterns. The lattice constants obtained from this analysis were verified by Le Bail fitting (Tables S8-S9). Analysis of the simulated unit cells revealed that, following activation, NU-1303-6 transitions to a lower symmetry crystal system, which results in peak splitting.

The final de-interpenetrated NU-1303-1 boasts remarkable porosity. Calculated nitrogen uptake values for NU-1303-1 reveal a higher expected geometric surface area of $5700\text{ m}^2\text{g}^{-1}$ and a record high calculated 96.6% free volume and $9.2\text{ cm}^3\text{g}^{-1}$ pore volume ($\text{H}^{*0.9}\text{K}^{*0.1}$ cation) of any MOF reported to date (Tables S4-S5)²⁹. While only 27% of the BET area and 24% of the free volume is accessed experimentally, we attribute this to partial pore collapse²⁰. Calculated geometric surface areas and pore volumes for NU-1303-6 compared to NU-1303-1 reveal that both values increase after de-interpenetration (Tables S4-S5), which is consistent with the literature³⁰. We experimentally demonstrate the differences in pore volume between NU-1303-6 and NU-1303-1 through thermogravimetric analysis (Fig. S14, Table S6).

Charged Point-Point Repulsions Drive Spontaneous De-Interpenetration

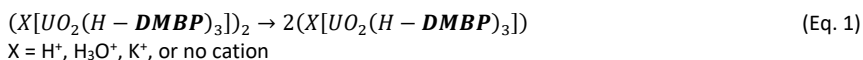
Since no external stimuli propel de-interpenetration, we reasoned that an interaction inherent to the system itself must drive de-interpenetration. Because NU-1303-6 is 6-fold interpenetrated, it has a high density of closely spaced uranium nodes (Fig. 1E); the closest U–U distance is 8.1 \AA (*M2*), and equatorial O atoms in *M2* are only separated by 3.7 \AA (Fig. S45). Additionally, each node holds a -1 formal charge, and uranium atoms possess relatively diffuse electron clouds. Thus, we hypothesized that energetically unfavored charged point-point repulsions (CPPR) between closely positioned anionic nodes on different networks drive NU-1303-6 de-interpenetration.

To investigate this hypothesis, we performed a density functional theory (DFT) energy decomposition analysis (EDA) using the Amsterdam Density Functional software (ADF 16.0)³¹ on *M1* and *M2* (Fig. S21). We developed *M1* and *M2* cluster models (Fig. S17), where each motif is composed of a pair of fragments, with each fragment comprising a uranyl node and three attached linkers capped with protons ($[\text{UO}_2(\text{H-DMBP})_3]^{-}$). We then determined the interaction energy (ΔE_{int}) between fragments in *M1* and *M2* at varying U–U distance in the gas phase, using the M06-2X density functional³².

ΔE_{int} is positive for both motifs over the range of investigated U–U distances (Fig. 3A), corroborating our hypothesis that node–node interactions are repulsive and energetically unfavored. For *M1*, ΔE_{int} is positive at close U–U distance and reaches a local minimum energy that is still positive (repulsive) at 10.4 \AA . This compares well to the experimental 9.7 \AA U–U distance. ΔE_{int} for *M2* is also positive at close U–U distance, with a positive local minimum energy at 8.6 \AA , well within reasonable error of the experimental 8.1 \AA U–U distance. ΔE_{int} for both *M1* and *M2* then moves towards zero at U–U distances reaching 50 \AA (Fig. S21A), indicating no interaction between fragments. At the predicted 10.4 \AA local minimum for *M1*, the total bonding energy is 9.3 kcalmol^{-1} , while it is 19.9 kcalmol^{-1} for *M2* at 8.2 \AA (Fig. 3A, inset). These positive ΔE_{int} values at local minimum energy U–U distances highlight that neither motif is energetically favored, and U–U repulsions dominate the electronic energy landscape in NU-1303-6. Since *M2* exhibits a more positive ΔE_{int} at its local

minimum, we conclude that in gas phase, *M2* is the less energetically favored motif. This is due to the closer distance between *M2* nodes and resulting steric hindrance (Fig. S21C).

The positive ΔE_{int} values for both motifs also suggest the formation of NU-1303-1 is energetically favored. Further DFT-computed free energies for the transformation of NU-1303-6 to NU-1303-1 establish that NU-1303-1 is thermodynamically favored, and that de-interpenetration occurs spontaneously. We calculated free energies of transformation by modeling de-interpenetration of the fragment pairs in the *M1* and *M2* cluster models into their independent fragments (Fig. S22, Table S11). To account for potential shielding of anionic nodes by counter-cations, we included either H^+ , H_3O^+ , or K^+ cations in our *M1* and *M2* cluster models, as well as a model with no cations (Eq. 1, Figs. S17-S20).



Because of different possible cation positions around the uranyl nodes, we report two stable configurations for *M2*: *M2a* and *M2b*. Using Eq. 2, we obtained free energies of transformation per uranium for *M1*, *M2a*, and *M2b*.

$$\Delta G \text{ per } U = \frac{2 * G_{NU-1303-1} - G_{NU-1303-6}}{2} \quad (\text{Eq. 2})$$

These calculations were performed in the presence of DMF, using the implicit Solvent Model based on Density (SMD)³³ and the M06-2X functional. For *M1*, *M2a*, and *M2b* in the presence of H^+ (Fig. 3B: orange bars), H_3O^+ , K^+ , or no cation (Fig. S23), the free energy is negative, indicating that the transformation of NU-1303-6 to NU-1303-1 is thermodynamically favorable and spontaneous. This can be attributed to unfavorable CPPR between anionic uranyl nodes. We note that CPPR is not observed to fully dissolve all six networks of NU-1303-6, since bulk NU-1303-1 is still observed after 752 days of soaking in DMF (Fig. S34), and single-crystals of NU-1303-1 are observed after 946 days of soaking in DMF.

Charged Point-Point Repulsion vs. Bridging Hydrogen-Bonded Water

We observed that under humid conditions, the NU-1303-6 de-interpenetration timeframe slows. We also noted that the 3.7 Å distance between equatorial oxygen atoms from different nodes in *M2* (Fig. S45) forms the optimally-sized pocket to house a water molecule. Coupling these two observations, we reasoned that water from humid atmospheric conditions may interact with neighboring nodes in *M2* to stabilize NU-1303-6 against de-interpenetration. Upon close inspection of the NU-1303-6 single-crystal structure, we detected a water molecule hydrogen-bonded between the equatorial oxygen atoms of the two nodes in *M2* (Fig. 4A). We did not observe similar behavior in *M1*. Hydrogen-bonding between two interpenetrated networks *via* a single water molecule likely occurs in *M2* because of the closer distance between uranium nodes. Conversely, the separation of nodes is 1.6 Å greater in *M1*, preventing a water molecule from hydrogen-bonding to two distinct networks.

To corroborate the stabilizing effect of hydrogen-bonded water molecules on de-interpenetration, we calculated free energies of transformation per uranium for *M1*, *M2a*, and *M2b* in the presence of water and different cations, using the implicit SMD solvent model for water. As expected, replacing implicit DMF solvent with water results in less-negative free-energies of de-interpenetration (Fig. 3B: blue bars). Similar trends were also observed in *M1*, *M2a*, and *M2b* models with other cations and with no cations (Fig. S23, Table S10). Hydrogen-bonded water thereby interacts with NU-1303-6 nodes to stabilize against de-interpenetration.

Thus, two competing interactions are at play in this system: CPPR vs. bridging hydrogen-bonded water (Fig. 4). In NU-1303-6, we experimentally observe a water molecule in *M2* bridging anionic uranium nodes on two different networks, creating favorable hydrogen-bonding interactions, and holding the interpenetrated frameworks together (Fig. 4A). However, CPPR favors de-interpenetration, and in the absence of water, (Fig. 4B) it drives the interpenetrated lattices apart (Fig. 4C). To further support this hypothesis, we soaked NU-

1303-6 in anhydrous solvent and activated it under anhydrous conditions to prevent water molecules from bridging neighboring networks and thus prevent NU-1303-6 from interpenetrating. Consistent with our hypothesis, under anhydrous conditions, nitrogen isotherms show that NU-1303-6 fully de-interpenetrates in four days (Fig. S37-S39, Table S3), 36 times faster than the original 144-day de-interpenetration. This observation demonstrates that CPPR drives the spontaneous de-interpenetration of NU-1303-6, making a material with more void space thermodynamically favored, while hydrogen-bonded water hinders de-interpenetration.

Experimental Control for Charged Point-Point Repulsion

To further validate the roles of CPPR and bridging water in de-interpenetration, we designed and synthesized a MOF named NU-1304. NU-1304 consists of the same anionic, uranyl-based node as NU-1303-6 (Fig. 1A) and a slightly modified linker: 2,2',6,6'-tetramethyl-biphenyl-4,4'-dicarboxylic acid (**TMBP**) (Figs. 5A, S3-S5, S41, Scheme S2). A combination of SCXRD and modeling with Topologically-Based Crystal Constructor (ToBaCCo)^{34,35} revealed the structure of NU-1304 to be the same *srs* topology and anionic, 6-fold interpenetrated framework as NU-1303-6 ($(\text{H}^{+}_{0.9}\text{K}^{+}_{0.1}[\text{UO}_2(\text{TMBP})_{1.5}]^{-})$ or $(\text{H}_3\text{O}^{+})_{0.9}\text{K}^{+}_{0.1}[\text{UO}_2(\text{TMBP})_{1.5}]^{-}$, Figs S40-S44, S46-S48, Table S2, Supplemental Data: NU-1304_Upositions). Analogous to NU-1303-6, NU-1304 also has two reoccurring motifs (*M3* and *M4*). *M3* spatially orients in a parallel arrangement, similar to *M1*, and *M4* in a perpendicular arrangement, similar to *M2* (Fig. S43). NU-1304 shows an analogous isotherm shape as NU-1303-6, with steps at $P/P_0 = 0.0071$ and 0.0601 (Fig. 5B, orange circles); these steps correspond to cages of 12.6 Å and 18.7 Å (Fig. 5C, orange trace) and match well with the NU-1304 structure (Fig. S43B). NU-1304 exhibits a BET area of $1570 \text{ m}^2\text{g}^{-1}$ and a pore volume of $0.77 \text{ cm}^3\text{g}^{-1}$ (Fig. S49, Table S3). In line with NU-1303-6, although the experimental PXRD of NU-1304 before activation matches well with the simulated PXRD from the NU-1304 structural model, it exhibits peak splitting after activation (Fig. 5D). As described above, post-activation peak splitting in this system indicates interpenetration. Similar to the case of NU-1303-6, we generated PXRD patterns and structural models (Supplemental Data: NU-1304_EtOH and NU-1304_Act) which matched the experimental PXRD patterns of NU-1304 after activation (Figs. 5D, S54). These revealed that peak splitting signaled a transition to lower crystal symmetry, and we verified the obtained lattice constants through Le Bail fitting (Tables S9, S13). Taken together, this data shows NU-1304 to be an interpenetrated MOF.

While NU-1303-6 and NU-1304 are isorecticular MOFs, the added methyl substituents in NU-1304 create greater steric hindrance between networks. As a result, the nodes in *M3* and *M4* separate by a greater distance than in *M1* and *M2*, such that the U–U distance in *M3* is 10.2 Å, and in *M4* it is 9.6 Å (Fig. S43C-D). We note that even the closest U–U distance present in NU-1304 (*M4*) remains 1.5 Å larger than that of NU-1303-6 (*M2*, Figs. 5A, S45). Since NU-1304 is isorecticular to NU-1303-6, with the one distinction being the distance between closest anionic nodes, NU-1304 is a valuable control material to study the role of CPPR in de-interpenetration.

Because the closest distance between anionic nodes on neighboring networks in NU-1304 is 1.5 Å larger than that of NU-1303-6 (Figs. 5A, S45), less-effective CPPR between nodes is expected. Since CPPR is the driving force for spontaneous de-interpenetration, we thus anticipated that NU-1304 would not exhibit de-interpenetration to the extent of NU-1303-6. Indeed, even after 1057 days of soaking in hydrous DMF (913 days longer than NU-1303-6) and 10 days of soaking in anhydrous DMF to account for any potential hydrogen-bonded water molecules bridging networks together and favoring interpenetration (6 days and 2.5 times longer than NU-1303-6, Figs. 5B-C, S50-S52, Table S3), nitrogen isotherms still reveal that NU-1304 remains interpenetrated. Additionally, the PXRD of NU-1304 shows splitting of the first two major peaks following activation (Figs. 5D, S53-S54). Similar to NU-1303-6, peak splitting after activation indicates the presence of interpenetration, and the absence of splitting suggests that fewer networks are present (Table S13). As such, we find that NU-1304 remains interpenetrated under the same conditions that lead to de-interpenetration in the structurally analogous NU-1303-6.

While researchers commonly add bulky functional groups to organic linkers to prevent interpenetration²¹, we observe the opposite trend with NU-1304. We attribute this exceptional behavior to less-effective CPPR, which is consistent with the NU-1304 de-interpenetration free energy calculations in the presence of implicit solvent. Free energy calculations were performed in the presence of no cations and in the presence of H⁺, H₃O⁺, and K⁺ cations (Figs. 5E, S55-S56, Table S14). Much like NU-1303-6, the different possible cation positions around the uranyl nodes resulted in two stable configurations for M4: M4a and M4b (analogous to M2a and M2b). In contrast to M1, M2a, and M2b in NU-1303-6 (Fig. 5E: solid bars), M3, M4a and M4b in NU-1304 possess more positive free-energy values (Fig. 5E: striped bars). Indeed, the added stabilization energies for M3, M4a and M4b are 5.4, 3.6, and 2.4 (implicit DMF), and 3.8, 2.9, and 0.9 (implicit water) kcalmol⁻¹, respectively. Similar results were also observed in the presence of H₃O⁺, K⁺, and no cations (Fig. S57). These findings indicate that NU-1304 is more stabilized against de-interpenetration than NU-1303-6 due to less effective CPPR. Taken together, the exceptional spontaneous de-interpenetration behavior of NU-1303-6 is attributed to CPPR between closely spaced anionic nodes.

In conclusion, we have discovered spontaneous de-interpenetration driven by charged point-point repulsions (CPPR), which reverse the universal thermodynamics of stability arising from reduction of porosity and enable the thermodynamic synthesis of highly porous materials. We demonstrate this phenomenon within an anionic, 6-fold interpenetrated MOF, NU-1303-6, with closely positioned, charged uranyl nodes, using crystallography, gas physisorption, and DFT calculations. As a result of CPPR, non-interpenetrated NU-1303-1 with a record high void fraction (96.6%) and pore volume (9.2 cm³g⁻¹) spontaneously forms as the thermodynamic product from the deintercalation of NU-1303-6.

Electrostatic interactions are an important fundamental behavior observed throughout multiple scientific disciplines and processes. By incorporating these fundamental interactions into synthetic materials and utilizing them as a functional tool to perform work, energetically demanding phenomena can be readily realized. In this report, we have demonstrated how repulsions of anionic points spontaneously generates useful void space through de-interpenetration. However, in principle, design considerations could be made to employ either anionic or cationic electrostatic interactions in any type of framework, where not only the node, but even the linker, counterion, or other charged groups embedded into the network material drive de-interpenetration. Thus, we expect that the detailed energetic understanding of CPPR and the de-interpenetration phenomenon developed here could be widely generalized for the direct and systematic production of non-interpenetrated structures which self-generate an abundance of valuable pore space. For instance, recent reports have shown how uranium catalyzes nitrogen fixation^{36,37}, which could likely be enhanced in a highly porous material. More fundamentally, this discovery compels a re-evaluation of the thermodynamics of porosity and will inspire an exploration of highly porous molecular systems.

EXPERIMENTAL PROCEDURES

Resource availability

Lead Contact

Further information and requests for resources should be directed to and will be fulfilled by the lead contact, Omar K. Farha (o-farha@northwestern.edu).

Materials Availability

All materials generated in this study are available from the lead contact without restriction.

Data and Code Availability

NU-1303-6, and NU-1303-3 X-ray crystallographic data can be found as Supplemental Data and have been deposited at the Cambridge Crystallographic Data Centre (CCDC), under deposition numbers CCDC 2050153 and 2050154, respectively. These data can be obtained free of charge from the CCDC via www.ccdc.cam.ac.uk. The following additional CIFs can also be found in the Supplemental Data: NU-1303-6_EtOH, NU-1303-6_Act, NU-1303-1_Upositions, NU-1303-1_Model, NU-1304_Upositions, NU-1304_ToBaCCo, NU-1304_EtOH,

and NU-1304_Act. The code used for PXRD pattern matching is available at https://github.com/rytheranderson/XRD_matching, and the code versions used are given in Table S7. All other relevant data supporting the findings of this study is available in the main text or the Supplemental Information.

Methods

NU-1303-6 Single-Crystal X-ray Diffraction (SCXRD)

A single-crystal was mounted directly from the mother liquor onto a MiTeGen loop on a Bruker Kappa diffractometer equipped with a micro-focus CuK α source (MX optics) and an APEX CCD area detector at 200 K. The temperature of the crystal was controlled with an Oxford Cryosystems low-temperature device. Data reduction was performed with the SAINT and APEX software using a multi-scan absorption correction. The structure was solved with the SHELXS³⁸ structure solution program using direct methods and by using Olex2³⁹ as the graphical interface. The model was refined with SHELXL⁴⁰ using least squares minimization.

NU-1303-3 SCXRD

A single-crystal was mounted directly from the mother liquor onto a MiTeGen loop on a Bruker Kappa diffractometer equipped with a micro-focus CuK α source (MX optics) and an APEX CCD area detector at 250 K. The temperature of the crystal was controlled with an Oxford Cryosystems low-temperature device. Data reduction was performed with the CrysAlisPro software using an empirical absorption correction with spherical harmonics. Using Olex2, the structure was solved with the SHELXT⁴¹ structure solution program using Intrinsic Phasing and refined with the SHELXL refinement package using Least Squares minimization.

NU-1303-1 SCXRD

Intensity data of a cubic single-crystal was collected at 200 K. The crystal was mounted on a MiTeGen loop with paratone oil on an XtaLAB Synergy diffractometer equipped with a micro-focus sealed X-ray tube PhotonJet (Cu) X-ray source and a Hybrid Pixel Array Detector (HyPix). The temperature of the crystal was controlled with an Oxford Cryosystems low-temperature device. Data reduction was performed with the CrysAlisPro software using an empirical absorption correction. The structure was solved with the ShelXS structure solution program using the direct methods solution method and by using Olex2 as the graphical interface. The model was refined with ShelXL using least squares minimization.

NU-1304 SCXRD

A single-crystal was mounted on MicroMesh (MiTeGen) in paratone oil and transferred to the cold gas stream (100 K) of a Bruker APEX II CCD area detector equipped with a MoK α I μ S micro-source with MX optics. Data integration and reduction were performed using the Bruker SAINT program in APEX2. Absorption correction was performed by multi-scan methods using SADABS⁴². The uranium atom positions were determined by *ab initio* methods (SHELXD⁴³) and refined by full-matrix least-squares refinement on F^2 (SHELXL) using the Yadokari-XG software package⁴⁴.

Optical Images

Optical images were acquired with a Nikon SMZ1500 microscope.

Powder X-Ray Diffraction (PXRD)

PXRD data was obtained using a Stoe STADI P and a Stoe STADI MP diffractometer, both of which were equipped with a CuK α 1 source and a 1D strip detector. Transmission mode was used for all samples measured after activation, and Debye-Scherrer mode was used for all capillary samples measured in solvents. Samples measured in Debye-Scherrer mode were prepared in 1 mm borosilicate glass capillaries (Charles Supper) in their respective solvents. A 0.7 mm borosilicate glass capillary was placed in the 1 mm glass capillary once the sample was loaded and secured with wax to prevent the packed sample from being displaced during the measurement. Samples measured in Debye-Scherrer mode for Le Bail fitting were prepared in 0.8mm Kapton capillaries in their respective solvents.

PXRD Matching Procedure

Simulated PXRD patterns were matched to their corresponding experimental PXRD patterns by varying the lattice parameters of the simulated unit cells to maximize peak overlap between the two patterns. First, the background was removed from the experimental patterns by modeling each peak with a Gaussian function of the correct height and a standard deviation of 0.05. Peaks were identified in the experimental patterns using the *signal.find_peaks* algorithm from the *SciPy Python* package, and only peaks with a minimum width of 5 points and a prominence of 0.05 (intensity units) were considered. We checked manually that all visually discernable peaks were successfully identified using this scheme. Next, the simulated PXRD pattern was matched to its corresponding experimental pattern by maximizing the overlap between the two patterns as a function of the simulated lattice parameters. The optimization was performed using differential evolution as implemented in the *scipy.optimize Python* package. Pattern overlap was determined by the city block distance between the simulated and experimental patterns. A population size of 20 with a recombination rate of 0.80 and a “randtobest1bin” strategy were used during differential evolution. All other differential evolution parameters corresponded to the defaults of the *scipy.optimize.differential_evolution* function. Each simulated pattern was generated using the *pymatgen.analysis.diffraction.xrd Python* package, and each peak was modeled with a Gaussian function of the simulated height and a standard deviation of 0.05. Patterns with split first peaks were matched under the constraints $a = b$ and $\alpha = \beta = \gamma = 90^\circ$. Patterns with single first peaks were matched under the constraints $a = b = c$ and $\alpha = \beta = \gamma = 90^\circ$.

Le Bail Fitting

Le Bail fittings were performed with GSAS-II (version 4917). Background (up to 10 parameters) and cell constants were freely refined. Most profile parameters were fixed based on the values obtained by fitting LaB6 (NIST 660c) except for the Gaussian U and Lorentzian Y parameters of each sample.

Topologically Based Crystal Constructor (ToBaCCo) NU-1304 Modeling Procedure

Our model of NU-1304 was constructed using the Topologically Based Crystal Constructor (ToBaCCo)^{34,35}. The NU-1304 linkers were added while maintaining the experimentally determined uranium node positions. The linker atom positions were then optimized according to the DFT linker optimization and the CIF generation procedure described below.

Density Functional Theory (DFT) Linker Optimization and CIF Generation

Energy-minima linker geometries for the NU-1303-6 and NU-1304 structures, under the geometry constraints imposed by the lattice parameters determined by the PXRD matching procedure outlined above, were determined according to the following procedure. First, for each MOF, all linkers of unique length and position relative to the two connected metal nodes were identified and extracted, including the two uranium nodes, where the two additional linker sites on each uranium node were capped with formate, according to the DFT optimized geometry of the node with all formate caps. Next, each of these extracted clusters was optimized using DFT (Gaussian16⁴⁵) with all linker atoms allowed to move and the metal/formate cap atom positions kept fixed. The B3LYP/6-31G* functional/basis set^{46,47} was used for all non-metal atoms. The B3LYP/SDD functional/basis set with the SDD ECP was used for uranium atoms. Keeping the nodes fixed in this manner ensured that the relative linker/node orientations were maintained. The DFT optimized linkers were then added back into their original position in each MOF.

Supercritical CO₂ (sc-CO₂) Activation

sc-CO₂ activation²⁶ was performed on a Tousimis Samdri PVT-3D critical point dryer, using either a CO₂ syphon or bone-dry CO₂ syphon tank. A previously reported procedure was followed⁴ with several modifications. Before activation, the sc-CO₂ unit chamber was rinsed with the same solvent used for the most recent MOF soak. The sample was quickly transferred from its sealed tube to a Tousimis “small particle holder” and into the sc-CO₂ unit. Since Tousimis “small particle holders” with 2 μ m mesh sizes were used to contain the sample, 3 mL of the MOF soaking solution was placed into the unit along with the MOF sample in order to keep the MOF covered in solvent at all times. The unit was cooled slowly (~2° C/minute) and filled with CO₂ (l) once 10° C was reached. An initial 20-minute purge was performed. Then,

four cycles of a 2-hour soak/3-minute purge were performed. Finally, the unit was heated to $\sim 40^\circ\text{C}$ and set to bleed overnight at 0.5 ccg^{-1} .

Thermal Activation

Thermal activation was performed under ultrahigh vacuum using a Micromeritics Smart VacPrep (SVP) instrument.

Nitrogen Physisorption

Nitrogen isotherms were collected at 77 K on a Micromeritics Tristar II 3020 and analyzed using the Brunauer–Emmett–Teller (BET) theory²⁷. The nonlocal density functional theory (NLDFT)⁴⁸ model for pillared clay was used to determine pore size distributions.

Nuclear Magnetic Resonance (NMR)

^1H spectra of **DMBP-OEt**, **DMBP** and $^{13}\text{C}\{^1\text{H}\}$ spectra of **TMBP-OEt** were collected on an Ag500, Bruker Avance III 500 MHz instrument. ^1H spectra of **TMBP**, **TMBP-OEt**, and digested NU-1303-6 and NU-1304 were collected on an A600, Bruker Avance III 600 MHz instrument.

Microwave Reactor

Linker synthesis and acid digestions for inductively coupled plasma-optical emission spectrometry experiments were performed on a Biotage Initiator+ microwave reactor (software version 2.3, build 6250).

Inductively Coupled Plasma-Optical Emission Spectrometry (ICP-OES)

Quantification of U and K was accomplished using ICP-OES of acid digested samples. Specifically, 2–4 mg of solid samples were digested in 2.5 mL concentrated trace nitric acid and microwaved at 200°C for 15 minutes. Ultra-pure H_2O ($18.2\text{ M}\Omega\text{-cm}$) was added to produce a final solution of 3.0% nitric acid (v/v) in a total sample volume of 10 mL. Quantitative standards were made using a $100\text{ }\mu\text{g mL}^{-1}$ U elemental standard and a $1000\text{ }\mu\text{g mL}^{-1}$ K elemental standard which were used to create a $20\text{ }\mu\text{g g}^{-1}$ U calibration standard and a $5\text{ }\mu\text{g g}^{-1}$ K calibration standard in 3.0% nitric acid (v/v). ICP-OES was performed on a computer-controlled (QTEGRA software) Thermo iCap7600 ICP-OES (Thermo Fisher Scientific, Waltham, MA, USA) operating in axial view and equipped with an ESI SC-2DX PrepFAST autosampler (Omaha, NE, USA). Online dilution was also carried out by the PrepFAST system and used to generate calibration curves consisting of 20, 10, 5, 1 and $0.5\text{ }\mu\text{g g}^{-1}$ U and 5, 2.5, 1 and $0.5\text{ }\mu\text{g g}^{-1}$ K. Each sample was acquired using 5 second visible exposure time and 15 second UV exposure time, running 3 replicates. The spectral lines selected for analysis were as follows: U (367.01, 385.96, 263.55 and 409.01 nm) and K (766.49 and 769.90 nm).

Inductively Coupled Plasma-Mass Spectrometry (ICP-MS)

Quantification of uranium (U) was accomplished using ICP-MS. Specifically, 50 μL aliquots were isolated from a soaking solution of NU-1303-6 in DMF. Ultra-pure H_2O ($18.2\text{ M}\Omega\text{-cm}$) and nitric acid were added to produce a final solution of 3.0% nitric acid in a total sample volume of 10 mL. A quantitative standard was made using a $100\text{ }\mu\text{g mL}^{-1}$ U elemental standard which was used to create a 200 ng g^{-1} U standard in 3.0% nitric acid (v/v) in a total sample volume of 50 mL. A solution of 3.0% nitric acid was used as the calibration blank.

ICP-MS was performed on a computer-controlled (QTEGRA software) Thermo iCapQ ICP-MS (Thermo Fisher Scientific, Waltham, MA, USA) operating in STD mode and equipped with a ESI SC-2DX PrepFAST autosampler (Omaha, NE, USA). Internal standard was added inline using the prepFAST system and consisted of 1 ng mL^{-1} of a mixed element solution containing Bi, In, ^6Li , Sc, Tb, Y (IV-ICPMS-71D from Inorganic Ventures). Online dilution was also carried out by the prepFAST system and used to generate a calibration curve consisting of 200, 100, 50, 10, and 2 ppb U. Each sample was acquired using 1 survey run (10 sweeps) and 3 main (peak jumping) runs (40 sweeps). The isotopes selected for analysis were ^{238}U and ^{89}Y , ^{115}In , ^{159}Tb (chosen as internal standards for data interpolation and machine stability). Instrument performance is optimized daily through autotuning followed by verification *via* a performance report (passing manufacturer specifications).

Ultraviolet-Visible Spectroscopy (UV-Vis)

Approximately 5 mg of NU-1303-6 was soaked in 1 mL DMF and left in a capped quart cuvette, which was sealed well with parafilm to prevent solvent loss. Since the MOF particles settled at the bottom of the cuvette, UV-Vis spectra was collected of the DMF solution at different time points. An initial baseline collection was performed with pure DMF solution which was subtracted from the following measurements. Diffuse reflectance UV-Vis spectra of the DMF solution was then recorded with a Shimadzu UV-2600 with a Harrick Praying Mantis diffuse reflectance accessory. We implemented a scan range from 200-800 nm with a data interval of 1.0 nm.

Thermogravimetric Analysis (TGA)

TGA experiments were performed using a TGA/DSC 1 LF (Mettler Toledo) instrument with STARe (v16.10) software. Samples were heated from 30 to 600 °C at 10 °C/min under N₂ in a 100 uL aluminum pan.

Pore Size Distribution (PSD), Geometric Surface Area, and Void Fraction Calculations

These calculations were performed using RASPA 2.0⁴⁹ with framework non-metal atom radii according to the Dreiding forcefield⁴⁹ and uranium atom radii according to the Universal Force Field⁴⁹. The geometric surface area for NU-1303-6 was calculated using RASPA (Monte Carlo code) with a N₂ sized probe (Table S4), and the void fraction was calculated using RASPA (Monte Carlo code) with a He sized probe (Table S5). The calculated pore volume was obtained by multiplying the void fraction by the cell volume.

Periodic Density Functional Theory (DFT) Optimization

Periodic DFT calculations were performed using the Vienna Ab initio Simulation Package (VASP 5.3.5)⁵⁰ Perdew–Burke–Ernzerhof (PBE) functional along with Grimme's D3 dispersion correction with Becke–Johnson damping which was used for structural optimization. A planewave energy cutoff of 400 eV, energy convergence criteria of 10⁻⁵ eV, and force convergence criteria of 0.05 eV/Å were used for all the calculations. The Brillouin zone was sampled using a Γ only k -point grid.

Energy Decomposition Analysis (EDA)

The EDA of the total interaction energy (ΔE_{int}) for $M1$ and $M2$ was performed in Amsterdam Density Functional (ADF) 2016 software³¹. Cluster models were extracted from the CIF of NU-1303-6 and truncated using a capping proton to form -COOH groups (Fig. S1). Minnesota's M06-2X density functional³² was employed for the fragment analysis along with the scalar relativistic zeroth order regular approximation (ZORA) with all electron Slater type basis sets of TZP quality. A Voronoi integration scheme with 6.0 significant digits was used for the numerical integrations. The 'Good' quality 'Zlm Fit' density fitting with radial spline functions and real spherical harmonics was employed. No symmetry was imposed in the ADF calculations.

Free Energy Cluster DFT Calculations

Free energy of transformation density functional theory (DFT) calculations for NU-1303-6 were performed on both cation-capped and uncapped cluster models extracted from the respective CIFs in Gaussian 16 software⁴⁵ using Minnesota's M06-2X functional³². Three capping cations (H⁺, H₃O⁺, and K⁺) were studied. For geometry optimization and frequency calculations, the uranyl node, capping cations, and carboxylate groups of the linkers coordinating equatorially to the node were relaxed while the positions of all other linker atoms were held fixed (Figs. S17-S20, S56). A def2TZVP basis set for the relaxed atoms excluding uranium, the Stuttgart-Dresden SDD/SDD basis set/pseudopotential for uranium, and a def2SVP basis set for all other frozen atoms of the linkers were employed. Each linker in the cluster model was truncated using a proton to form a -COOH group to retain its interaction with the methyl group of the other linker. An ultrafine grid was employed for performing the numerical integrations. Vibrational frequencies were computed at the optimized geometries for calculating the free energies and for determining the nature of the stationary point. The optimized structures had all real vibrational frequencies. Vibrational frequencies below 50 cm⁻¹ were corrected to 50 cm⁻¹ while computing thermal corrections to free energies. The effect of the implicit solvent was studied by using the implicit SMD

solvation model³³ for DMF (N,N-dimethylformamide) and water respectively. The uranium atom has a +6 oxidation state, and hence, all calculations were performed in the singlet state with one negative charge per node+linker motif.

SUPPLEMENTAL INFORMATION

The Supplemental Information file contains Materials, Supplemental Experimental Procedures, Supplemental Schemes, Supplemental Figures, Supplemental Tables, and Supplemental References

Full crystallographic information files for NU-1303-6 and NU-1303-3

Crystallographic information files for the uranium positions of NU-1303-1 (NU-1303-1_Upositions) and NU-1304 (NU-1304_Upositions)

Simulated crystallographic information files for NU-1303-6_EtOH, NU-1303-6_Act, NU-1303-1_Model, NU-1304_EtOH, NU-1304_Act, and NU-1304_ToBaCCo

Optimized Cartesian coordinates for NU-1303-6 and NU-1304 cluster models

ACKNOWLEDGMENTS

O.K.F., S.L.H., S.C., D.R., Peng L., J.G.K., and L.G. acknowledge support from the U.S. Department of Energy, National Nuclear Security Administration, under Award Number DE-NA0003763. D.A.G.-G. acknowledges funding from NSF CAREER under Award Number CBET 1846707. K.O., T. I., and X. Z. acknowledge support from the Inorganometallic Catalyst Design Center, an EFRC funded by the DOE, Office of Science, Basic Energy Sciences under award number DE-SC0012702. L.R. acknowledges support from the Air Force Research Laboratory (FA8650-15-2-5518). Penghao L. and J.F.S. thank Northwestern University (NU) for financial support. This work made use of the International Institute for Nanotechnology (IIN); IMSERC at Northwestern University, which has received support from the Soft and Hybrid Nanotechnology Experimental (SHyNE) Resource (NSF ECCS-2025633), the State of Illinois, Northwestern University, and the IIN; Northwestern University Quantitative Bio-element Imaging Center generously supported by NASA Ames Research Center Grant NNA04CC36G; the Mio supercomputer cluster maintained by the Colorado School of Mines where non-periodic DFT simulations (*i.e.* linker optimizations) were performed. S.L.H. acknowledges support from the International Institute for Nanotechnology (IIN) Ryan Fellowship and the U.S. Department of Energy National Nuclear Security Administration Stewardship Science Graduate Fellowship (DOE NNSA SSGF) under Award Number DE-NA0003960. J.G.K. (DGE-1842165), M.C.W. (DGE-1842165), and A.M.E. (DGE-1324585) are supported by the National Science Foundation Graduate Research Fellowship. S.L.H. thanks Louis R. Redfern, Chung-Wei Kung, and Riki J. Drout for scientific discussions during the entire project; Matthew G. Cowan, Nathaniel V. Nucci, Timothy D. Vaden, and Margaret E. Schott for manuscript review in the late stages of the project; Charlotte Stern for discussions regarding structure refinements; Kent Kirlikovali and Rodrigo Maldonado for advice regarding linker synthesis; Zhijie Chen for data visualization advice. We thank Joshua Zhu for assistance with anhydrous solvent, Marek Majewski for assistance with linker synthesis at the very early stage of the project, and Haoyuan Chen for performing a MOF database search.

AUTHOR CONTRIBUTIONS

O.K.F. supervised the project; S.L.H. and O.K.F. conceived the project and led the investigation. S.L.H., O.K.F., X.Z., and T.I. designed the experiments and interpreted the results, with help from J.G.K.; S.L.H. synthesized ligand and MOFs, performed MOF characterization, and conducted all activation, gas adsorption, and PXRD experiments, with help from J.G.K.; S.C. and D.R. designed the computational models and performed free energy of de-interpenetration density functional theory calculations as well as the energy decomposition analysis under the supervision of L.G.; R.A. performed PSD calculations, void fraction calculations, and geometric surface area calculations, under the supervision of D.A.G.; R.A. also performed ToBaCCo modeling, PXRD pattern matching, non-periodic DFT simulations (*i.e.* linker optimizations), and subsequent CIF generation with the help of K.Z.

under the supervision of D.A.G.; X. Z., C.D.M., J.G.K., and K.O. collected and analyzed single-crystal X-ray diffraction data, and C.D.M. performed Le Bail powder fitting; Peng L. performed Materials Studio modeling and assisted S.L.H. in MOF synthesis; Penghao L. synthesized ligand under the supervision of J.F.S.; X.W. and M.C.W. assisted S.L.H. with revision experiments. S.L.H., A.M.E. (under the supervision of W.R.D.), L.R., and O.K.F. wrote the manuscript, and all authors commented on and revised the manuscript.

DECLARATION OF INTERESTS

O.K.F. has a financial interest in NuMat Technologies, a startup company that is seeking to commercialize MOFs. All other authors declare no competing interests.

INCLUSION AND DIVERSITY

One or more of the authors of this paper self-identifies as an underrepresented ethnic minority in science. One or more of the authors of this paper self-identifies as a member of the LGBTQ+ community. One or more of the authors of this paper received support from a program designed to increase minority representation in science.

REFERENCES

1. Carlucci, L., Ciani, G., and Proserpio, D.M. (2003). Polycatenation, polythreading and polyknotting in coordination network chemistry. *Coord. Chem. Rev.* *246*, 247-289. [https://doi.org/10.1016/S0010-8545\(03\)00126-7](https://doi.org/10.1016/S0010-8545(03)00126-7).
2. Forgan, R.S., Sauvage, J.-P., and Stoddart, J.F. (2011). Chemical topology: complex molecular knots, links, and entanglements. *Chem. Rev.* *111*, 5434-5464. [10.1021/cr200034u](https://doi.org/10.1021/cr200034u).
3. Hasell, T., and Cooper, A.I. (2016). Porous organic cages: soluble, modular and molecular pores. *Nat. Rev. Mater.* *1*, 16053-16066. [10.1038/natrevmats.2016.53](https://doi.org/10.1038/natrevmats.2016.53).
4. Chen, Z., Li, P., Anderson, R., Wang, X., Zhang, X., Robison, L., Redfern, L.R., Moribe, S., Islamoglu, T., Gómez-Gualdrón, D.A., et al. (2020). Balancing volumetric and gravimetric uptake in highly porous materials for clean energy. *Science* *368*, 297-303. [10.1126/science.aaz8881](https://doi.org/10.1126/science.aaz8881).
5. Banerjee, D., Simon, C.M., Elsaidi, S.K., Haranczyk, M., and Thallapally, P.K. (2018). Xenon Gas Separation and Storage Using Metal-Organic Frameworks. *Chem* *4*, 466-494. [10.1016/j.chempr.2017.12.025](https://doi.org/10.1016/j.chempr.2017.12.025).
6. Dong, J., Zhang, K., Li, X., Qian, Y., Zhu, H., Yuan, D., Xu, Q.-H., Jiang, J., and Zhao, D. (2017). Ultrathin two-dimensional porous organic nanosheets with molecular rotors for chemical sensing. *Nat. Commun.* *8*, 1142-1155. [10.1038/s41467-017-01293-x](https://doi.org/10.1038/s41467-017-01293-x).
7. Koo, W.-T., Jang, J.-S., and Kim, I.-D. (2019). Metal-Organic Frameworks for Chemiresistive Sensors. *Chem* *5*, 1938-1963. [10.1016/j.chempr.2019.04.013](https://doi.org/10.1016/j.chempr.2019.04.013).
8. Lian, X., Fang, Y., Joseph, E., Wang, Q., Li, J., Banerjee, S., Lollar, C., Wang, X., and Zhou, H.-C. (2017). Enzyme-MOF (metal-organic framework) composites. *Chem. Soc. Rev.* *46*, 3386-3401. [10.1039/C7CS00058H](https://doi.org/10.1039/C7CS00058H).
9. McKinlay, A.C., Morris, R.E., Horcajada, P., Férey, G., Gref, R., Couvreur, P., and Serre, C. (2010). BioMOFs: metal-organic frameworks for biological and medical applications. *Angew. Chem. Int. Ed.* *49*, 6260-6266. <https://doi.org/10.1002/anie.201000048>.
10. Sheberla, D., Bachman, J.C., Elias, J.S., Sun, C.-J., Shao-Horn, Y., and Dincă, M. (2017). Conductive MOF electrodes for stable supercapacitors with high areal capacitance. *Nat. Mater.* *16*, 220-224. [10.1038/nmat4766](https://doi.org/10.1038/nmat4766).
11. Bavykina, A., Kolobov, N., Khan, I.S., Bau, J.A., Ramirez, A., and Gascon, J. (2020). Metal-organic frameworks in heterogeneous catalysis: recent progress, new trends, and future perspectives. *Chem. Rev.* *120*, 8468-8535. [10.1021/acs.chemrev.9b00685](https://doi.org/10.1021/acs.chemrev.9b00685).
12. Jiang, H.-L., Makal, T.A., and Zhou, H.-C. (2013). Interpenetration control in metal-organic frameworks for functional applications. *Coord. Chem. Rev.* *257*, 2232-2249. <https://doi.org/10.1016/j.ccr.2013.03.017>.

13. Ferguson, A., Liu, L., Tapperwijn, S.J., Perl, D., Coudert, F.-X., Van Cleuvenbergen, S., Verbiest, T., van der Veen, M.A., and Telfer, S.G. (2016). Controlled partial interpenetration in metal–organic frameworks. *Nat. Chem.* **8**, 250-257. 10.1038/nchem.2430.
14. Cao, J., Ma, W., Lyu, K., Zhuang, L., Cong, H., and Deng, H. (2020). Twist and sliding dynamics between interpenetrated frames in Ti-MOF revealing high proton conductivity. *Chem. Sci.* **11**, 3978-3985. 10.1039/C9SC06500H.
15. Kitagawa, S., Kitaura, R., and Noro, S.-i. (2004). Functional porous coordination polymers. *Angew. Chem. Int. Ed.* **43**, 2334-2375. doi:10.1002/anie.200300610.
16. Evans, J.D., Bon, V., Senkovska, I., Lee, H.-C., and Kaskel, S. (2020). Four-dimensional metal-organic frameworks. *Nat. Commun.* **11**, 2690. 10.1038/s41467-020-16527-8.
17. Furukawa, H., Cordova, K.E., O’Keeffe, M., and Yaghi, O.M. (2013). The chemistry and applications of metal-organic frameworks. *Science* **341**, 974-986. 10.1126/science.1230444.
18. Liang, W., Bhatt, P.M., Shkurenko, A., Adil, K., Mouchaham, G., Aggarwal, H., Mallick, A., Jamal, A., Belmabkhout, Y., and Eddaoudi, M. (2019). A Tailor-Made Interpenetrated MOF with Exceptional Carbon-Capture Performance from Flue Gas. *Chem.* <https://doi.org/10.1016/j.chempr.2019.02.007>.
19. Dolgoplova, E.A., Rice, A.M., and Shustova, N.B. (2018). Actinide-based MOFs: a middle ground in solution and solid-state structural motifs. *Chem. Commun.* **54**, 6472-6483. 10.1039/C7CC09780H.
20. Li, P., Vermeulen, N.A., Malliakas, C.D., Gomez-Gualdrón, D.A., Howarth, A.J., Mehdi, B.L., Dohnalkova, A., Browning, N.D., O’Keeffe, M., and Farha, O.K. (2017). Bottom-up construction of a superstructure in a porous uranium-organic crystal. *Science* **356**, 624-627. 10.1126/science.aam7851.
21. Zhang, X., Chen, Z., Liu, X., Hanna, S.L., Wang, X., Taheri-Ledari, R., Maleki, A., Li, P., and Farha, O.K. (2020). A historical overview of the activation and porosity of metal–organic frameworks. *Chem. Soc. Rev.* **49**, 7406-7427. 10.1039/D0CS00997K.
22. Eddaoudi, M., Kim, J., Rosi, N., Vodak, D., Wachter, J., Keffe, M., and Yaghi, O.M. (2002). Systematic design of pore size and functionality in isorecticular MOFs and their application in methane storage. *Science* **295**, 469-472. 10.1126/science.1067208.
23. Shekha, O., Wang, H., Paradinas, M., Ocal, C., Schüpbach, B., Terfort, A., Zacher, D., Fischer, R.A., and Wöll, C. (2009). Controlling interpenetration in metal–organic frameworks by liquid-phase epitaxy. *Nat. Mater.* **8**, 481-484. 10.1038/nmat2445.
24. Burns, P.C. (2005). U6+ minerals and inorganic compounds: insights into an expanded structural hierarchy of crystal structures. *Can. Mineral.* **43**, 1839-1894. DOI 10.2113/gscanmin.43.6.1839.
25. Hyde, S.T., O’Keeffe, M., and Proserpio, D.M. (2008). A short history of an elusive yet ubiquitous structure in chemistry, materials, and mathematics. *Angew. Chem. Int. Ed.* **47**, 7996-8000. <https://doi.org/10.1002/anie.200801519>.
26. Nelson, A.P., Farha, O.K., Mulfort, K.L., and Hupp, J.T. (2009). Supercritical processing as a route to high internal surface areas and permanent microporosity in metal–organic framework materials. *J. Am. Chem. Soc.* **131**, 458-460. 10.1021/ja808853q.
27. Brunauer, S., Emmett, P.H., and Teller, E. (1938). Adsorption of gases in multimolecular layers. *J. Am. Chem. Soc.* **60**, 309-319. 10.1021/ja01269a023.
28. Yuan, S., Zou, L., Qin, J.-S., Li, J., Huang, L., Feng, L., Wang, X., Bosch, M., Alsalmeh, A., Cagin, T., and Zhou, H.-C. (2017). Construction of hierarchically porous metal–organic frameworks through linker labilization. *Nat. Commun.* **8**, 15356. 10.1038/ncomms15356.
29. Hönicke, I.M., Senkovska, I., Bon, V., Baburin, I.A., Bönisch, N., Raschke, S., Evans, J.D., and Kaskel, S. (2018). Balancing mechanical stability and ultrahigh porosity in crystalline framework materials. *Angew. Chem. Int. Ed.* **57**, 13780-13783. 10.1002/anie.201808240.

30. Düren, T., Millange, F., Férey, G., Walton, K.S., and Snurr, R.Q. (2007). Calculating geometric surface areas as a characterization tool for metal–organic frameworks. *J. Phys. Chem. C* *111*, 15350-15356. [10.1021/jp074723h](https://doi.org/10.1021/jp074723h).
31. te Velde, G., Bickelhaupt, F.M., Baerends, E.J., Fonseca Guerra, C., van Gisbergen, S.J.A., Snijders, J.G., and Ziegler, T. (2001). Chemistry with ADF. *J. Comput. Chem.* *22*, 931-967. <https://doi.org/10.1002/jcc.1056>.
32. Zhao, Y., and Truhlar, D.G. (2006). A new local density functional for main-group thermochemistry, transition metal bonding, thermochemical kinetics, and noncovalent interactions. *J. Chem. Phys.* *125*, 194101-194118. [10.1063/1.2370993](https://doi.org/10.1063/1.2370993).
33. Marenich, A.V., Cramer, C.J., and Truhlar, D.G. (2009). Universal solvation model based on solute electron density and on a continuum model of the solvent defined by the bulk dielectric constant and atomic surface tensions. *J. Phys. Chem. B* *113*, 6378-6396. [10.1021/jp810292n](https://doi.org/10.1021/jp810292n).
34. Anderson, R., and Gómez-Gualdrón, D.A. (2019). Increasing topological diversity during computational “synthesis” of porous crystals: how and why. *CrystEngComm* *21*, 1653-1665. [10.1039/C8CE01637B](https://doi.org/10.1039/C8CE01637B).
35. Colón, Y.J., Gómez-Gualdrón, D.A., and Snurr, R.Q. (2017). Topologically guided, automated construction of metal–organic frameworks and their evaluation for energy-related applications. *Cryst. Growth Des.* *17*, 5801-5810. [10.1021/acs.cgd.7b00848](https://doi.org/10.1021/acs.cgd.7b00848).
36. Falcone, M., Barluzzi, L., Andrez, J., Fadaei Tirani, F., Živković, I., Fabrizio, A., Corminboeuf, C., Severin, K., and Mazzanti, M. (2019). The role of bridging ligands in dinitrogen reduction and functionalization by uranium multimetallic complexes. *Nat. Chem.* *11*, 154-160. [10.1038/s41557-018-0167-8](https://doi.org/10.1038/s41557-018-0167-8).
37. Falcone, M., Chatelain, L., Scopelliti, R., Živković, I., and Mazzanti, M. (2017). Nitrogen reduction and functionalization by a multimetallic uranium nitride complex. *Nature* *547*, 332-335. [10.1038/nature23279](https://doi.org/10.1038/nature23279).
38. Sheldrick, G. (1990). Phase annealing in SHELX-90: direct methods for larger structures. *Acta Crystallogr. A* *46*, 467-473. [doi:10.1107/S0108767390000277](https://doi.org/10.1107/S0108767390000277).
39. Dolomanov, O.V., Bourhis, L.J., Gildea, R.J., Howard, J.A.K., and Puschmann, H. (2009). OLEX2: a complete structure solution, refinement and analysis program. *J. Appl. Crystallogr.* *42*, 339-341. [doi:10.1107/S0021889808042726](https://doi.org/10.1107/S0021889808042726).
40. Sheldrick, G. (2015). Crystal structure refinement with SHELXL. *Acta Crystallogr. C* *71*, 3-8. [doi:10.1107/S2053229614024218](https://doi.org/10.1107/S2053229614024218).
41. Sheldrick, G. (2015). SHELXT - Integrated space-group and crystal-structure determination. *Acta Crystallogr. A* *71*, 3-8. [doi:10.1107/S2053273314026370](https://doi.org/10.1107/S2053273314026370).
42. Krause, L., Herbst-Irmer, R., Sheldrick, G.M., and Stalke, D. (2015). Comparison of silver and molybdenum microfocus X-ray sources for single-crystal structure determination. *J. Appl. Crystallogr.* *48*, 3-10. [doi:10.1107/S1600576714022985](https://doi.org/10.1107/S1600576714022985).
43. Schneider, T.R., and Sheldrick, G.M. (2002). Substructure solution with SHELXD. *Acta Crystallogr. D* *58*, 1772-1779. [doi:10.1107/S0907444902011678](https://doi.org/10.1107/S0907444902011678).
44. C. Kabuto, S.A., T. Nemoto, and E. Kwon (2009). Release of Software (Yadokari-XG 2009) for Crystal Structure Analyses. *J. Cryst. Soc. Jpn.* *51*, 218-224.
45. Frisch, M.J., Trucks, G.W., Schlegel, H.B., Scuseria, G.E., Robb, M.A., Cheeseman, J.R., Scalmani, G., Barone, V., Petersson, G.A., Nakatsuji, H., et al. (2016). Gaussian 16 Rev. C.01.
46. Becke, A.D. (1988). Density-functional exchange-energy approximation with correct asymptotic behavior. *Phys. Rev. A* *38*, 3098-3100. [10.1103/PhysRevA.38.3098](https://doi.org/10.1103/PhysRevA.38.3098).
47. Lee, C., Yang, W., and Parr, R.G. (1988). Development of the Colle-Salvetti correlation-energy formula into a functional of the electron density. *Phys. Rev. B* *37*, 785-789. [10.1103/PhysRevB.37.785](https://doi.org/10.1103/PhysRevB.37.785).
48. Landers, J., Gor, G.Y., and Neimark, A.V. (2013). Density functional theory methods for characterization of porous materials. *Colloids Surf. A: Physicochem. Eng. Asp.* *437*, 3-32. <https://doi.org/10.1016/j.colsurfa.2013.01.007>.
49. Mayo, S.L., Olafson, B.D., and Goddard, W.A. (1990). DREIDING: a generic force field for molecular simulations. *J. Phys. Chem.* *94*, 8897-8909. [10.1021/j100389a010](https://doi.org/10.1021/j100389a010).

50. Kresse, G., and Furthmüller, J. (1996). Efficient iterative schemes for ab initio total-energy calculations using a plane-wave basis set. *Phys. Rev. B* 54, 11169-11186. 10.1103/PhysRevB.54.11169.

FIGURE TITLES AND LEGENDS

Figure 1. NU-1303-6 Interpenetrated Structure from SCXRD

Schematic representation of NU-1303-6 (A) node and (B) biphenylene linker. Atom color scheme: carbon, gold; oxygen, orange; uranium, yellow. H atoms omitted for clarity. (C) One *srs* cage and representative pore size shown by orange sphere. (D) One *srs* network. (E) *M1* and *M2* with close U–U distances. (F) Representative pore sizes of NU-1303-6 shown by gray and blue spheres. Each network identified by a different color for clarity. (G) Six identical *srs* networks interpenetrate to form NU-1303-6.

Figure 2. De-interpenetration of NU-1303-6

(A, B, C) Topological representations of NU-1303-6, NU-1303-3, and NU-1303-1, respectively (D, F) Nitrogen adsorption-desorption isotherms for NU-1303-6 and NU-1303-1, respectively, at 77 K. Filled circles represent adsorption, and open circles represent desorption. (E) PXRD patterns (top to bottom) of experimental NU-1303-6 in DMF, simulated NU-1303-1, simulated NU-1303-3, and simulated NU-1303-6. (G, I) Pore-size distributions for NU-1303-6 and NU-1303-1, respectively. (H) PXRD patterns (top to bottom) of experimental activated NU-1303-1, simulated NU-1303-1, experimental activated NU-1303-6, and simulated activated NU-1303-6. See Fig. S16 for full range.

Figure 3. DFT Computation Reveals CPPR and Spontaneous Nature of De-interpenetration in NU-1303-6

(A) Total energy decomposition into ΔE_{int} using M06-2X functional at varying U–U distance. Inset shows energy values at the calculated minimum energy U–U distance for each motif in kcalmol⁻¹. (B) Free energy of transformation calculations of *M1*, *M2a*, and *M2b* in implicit solvent models for DMF (orange) and water (blue), in the presence of H⁺ cations.

Figure 4. Hydrogen-Bonded Water Bridges Networks Together and Hinders CPPR-Driven De-Interpenetration

(A) SCXRD structure of two uranium nodes in *M2* bridged together by a hydrogen-bonded water molecule. (B) Removing water in *M2* allows for CPPR between the anionic nodes to dominate. (C) CPPR causes de-interpenetration, resulting in one remaining anionic network.

Figure 5. De-Interpenetration Not Observed in NU-1304

(A) Biphenylene linkers and structures of *M2* (NU-1303-6) and *M4* (NU-1304). Portions of linkers are omitted and/or truncated for clarity. Crystallographically identified water molecule in *M2* and all H atoms are hidden for clarity. Atom color scheme: carbon, gold; oxygen, orange; uranium, yellow. (B) NU-1304 nitrogen adsorption-desorption isotherms after activation (orange circles) and after anhydrous activation (blue diamonds). Filled circles represent adsorption, and open circles represent desorption. (C) Pore-size distributions for NU-1304 after activation (orange) and after anhydrous activation (blue). (D) PXRD patterns (bottom to top) of simulated NU-1304, experimental NU-1304 in DMF, simulated activated NU-1304, experimental activated NU-1304, experimental activated NU-1304 (anhydrous conditions). (E) Free energy of de-interpenetration DFT calculations of *M1*, *M3*, *M2a*, *M4a*, *M2b*, and *M4b* in implicit solvent models for DMF (orange) and water (blue). This data is shown in the presence of H⁺ cations, using the M06-2X functional.

SUPPLEMENTAL EXCEL TABLE TITLES AND LEGENDS**Excel Spreadsheet 1. Optimized Cartesian Coordinates of NU-1303-6**

Optimized cartesian coordinates for the NU-1303-6 cluster models used for free energy calculations and energy decomposition analysis.

Excel Spreadsheet 2. Optimized Cartesian Coordinates of NU-1304

Optimized cartesian coordinates for the NU-1304 cluster models used for free energy calculations and energy decomposition analysis.